Frequency-Selective Cranial Resonance: Quantifying Cavity-Dependent Fields and Their Relationship to EEG Phase Metrics

ABSTRACT

We investigated frequency-selective cranial resonance using multichannel bone-conducted surface-acoustic-wave (SAW) recordings synchronized with EEG in 30 adults. Resonance patterns were cavity-dependent and anatomically constrained, with higher Resonance-Coherence Index (RCI) in mechanically coupled structures. Predictive Spectral Similarity (PSS) indicated short-term spectral predictability, while the Energy-Stability Index (ESI) reflected stable RMS envelopes over time. We observed a selectivity–speed trade-off: greater spectral selectivity (higher Q-factor) was associated with slower envelope rise (larger ΔLatency). After false-discovery-rate control, no significant sex differences were detected for RCI, PSS, ESI, Q, f_0, or ΔLatency. Sensitivity analyses supported robustness to window-length choices and artifact-rejection rules. Collectively, these findings suggest that cranial structures behave as a band-limited medium whose resonance features can be quantified reproducibly and studied alongside neural rhythms. The proposed pipeline provides a reproducible template for SAW–EEG research and motivates integrative models linking sinus geometry, airflow, tissue properties, and oscillatory activity. Stability indices (RCI/PSS/ESI) may offer non-invasive markers to characterize conductive pathways and inform acoustical interventions; future work should refine Q estimation, expand cohorts, and test task-evoked and interventional paradigms.

Introduction

Neural oscillations and inter-areal phase coordination are widely acknowledged as essential principles for large-scale brain integration, linking rhythmic dynamics to perception, attention, and cognition (Buzsáki, 2006; Varela, Lachaux, Rodriguez, & Martinerie, 2001). Phase-based indices—particularly the phase-locking value (PLV)—offer a principled, time-resolved quantification of phase alignment across channels in electrophysiological data (Lachaux, Rodriguez, Martinerie, & Varela, 1999). Beyond measurement, theoretical accounts propose that oscillatory coordination supports predictive, energy-efficient computation, placing synchrony within a broader functional framework (Friston, 2010).

Within this context, cranial-cavity mechanical resonance provides a complementary, bone-conducted macroscopic phenomenon that can be quantified alongside neural phase metrics. The skull and paranasal cavities form a coupled, frequency-selective resonant structure capable of supporting low-amplitude mechanical wave propagation with cavity-dependent transfer characteristics that are amenable to modeling and empirical verification (Padhye et al., 2019; Yang et al., 2020). Although mechanical resonance is not equivalent to neural synchrony, resonance features that are stable, anatomically constrained, and time-locked to EEG may offer a tractable route to probing physical pathways through which cranial structures could shape—or reflect—oscillatory dynamics at behaviorally relevant timescales.

We adopt the Enhanced Neuro-Oscillatory Synaptic Heuristic as a unified framework for analysis and simulation, linking resonance selectivity and stability to principles of oscillatory coordination. Using multichannel bone-conducted surface-acoustic-wave (SAW) recordings synchronized with EEG from 30 adults, we implement a standardized time–frequency pipeline to derive five complementary resonance metrics that summarize stability and selectivity: (i) a Resonance-Coherence Index (RCI) capturing the consistency of phase alignment across short windows, (ii) Predictive Spectral Similarity (PSS) between consecutive windows, (iii) an Energy-Stability Index (ESI) based on RMS variability, (iv) spectral selectivity quantified by Q-factor (−3 dB peak sharpness), and (v) envelope rise latency (ΔLatency; time-to-50% envelope). After harmonizing anatomical labels by cavity and side (frontal, maxillary, ethmoid, sphenoid; right/left), we summarize metrics by group and interpret them relative to established phase-based concepts (Lachaux et al., 1999; Varela et al., 2001) and broader theoretical perspectives (Friston, 2010).

We test three working hypotheses: (i) resonance patterns are cavity-specific and frequency-selective, with stronger coupling among anatomically adjacent regions (Buzsáki, 2006; Varela et al., 2001); (ii) higher Q-factor reflects greater spectral selectivity but entails a latency trade-off (larger ΔLatency), consistent with resonant transfer mechanics in cranial structures (Padhye et al., 2019; Yang et al., 2020); and (iii) the empirical topology of human measurements is consistent with the heuristic's simulation regime, motivating subsequent joint SAW–EEG validation and the development of neuro-acoustic biomarkers grounded in this framework.

Contributions. This study makes three primary contributions. First, we analyze synchronized multichannel SAW recordings time-locked to EEG in 30 adults with harmonized anatomical grouping by cavity and side. Second, we propose and apply a compact, reproducible metric set (RCI, PSS, ESI, Q-factor, and ΔLatency) to quantify resonance stability, predictability, energy consistency, spectral selectivity, and temporal dynamics within a standardized time–frequency pipeline. Third, we test cavity-specificity and a selectivity–speed trade-off and verify robustness to window-length choices and artifact-rejection rules, motivating follow-up SAW–EEG validation and biomarker development.

1. METHODOLOGY

A. PARTICIPANTS AND ELIGIBILITY

We enrolled 30 adult volunteers (men and women) Inclusion criteria: age ≥ 18 years; capacity to provide informed consent exclusion criteria: acute nasal/sinus infection; recent nasal surgery or trauma; and neurological conditions that could substantially affect EEG.

Demographics

Table 1. The cohort comprised 18 males (60.0%) and 12 females (40.0%).

Category	Count (N)	Percentage (%)
Male	18	60.0
Female	12	40.0
Total	30	100.0

2. Apparatus

SAW Placement and Isolation: Bone-conducted surface acoustic wave (SAW) sensors were placed to detect vibrations in the frontal, maxillary, ethmoid, and sphenoid sinus areas. A foam/gel layer and steady contact pressure helped reduce interference between cavities. EEG Configuration: Scalp EEG followed the international 10–20 system.

M1/M2 (left/right mastoids) were used for reference or extra recordings if needed. Time Alignment: A hardware trigger, like a TTL pulse or manual tap, was used at the start of recording for precise timing between SAW and EEG inputs. Front-end Agnosticism: The system was designed to work with any front-end, as long as it met the minimum sampling and bandwidth requirements below. Sampling and Filtering: The SAW sampling rate was at least 1 kHz. The EEG sampling rate was at least 500 Hz, preferably 1 kHz, to handle harmonics and phase measurements. Standard clinical/lab EEG bandwidths were used, and a notch filter at the local power-line frequency (50/60 Hz) was applied if needed.

Table 2. spec table

Subsystem	Sensor / Montage	Sampling	Analog Bandwidth	Notch
SAW (bone-conducted)	Per-cavity (frontal, maxillary, ethmoid, sphenoid) with decoupled mounts	≥ 1 kHz	Matches sensor response; ≥ 0.5–400 Hz recommended for cavity modes	50/60 Hz as needed
EEG (10–20)	Standard 10–20; M1/M2 available	≥ 500 Hz (1 kHz preferred)	Typical clinical/lab EEG (e.g., ~0.1–200/250 Hz)	50/60 Hz as needed
Synchronization	Hardware TTL/tap to both paths	—	—	—

3. Data acquisition

Multichannel SAW signals were recorded from the cranial and sinus regions using standardized placement. Each record included categorical labels for the cavity (frontal, maxillary, ethmoid, sphenoid) and, when applicable, the side (right/left). Before analysis, these labels were harmonized through a rule-based map (e.g., “Fron./Frnt”→Frontal; “Rt/R”→Right) to produce canonical levels (Frontal, Maxillary, Ethmoid, Sphenoid; Right, Left) suitable for group summaries and statistical testing. The mechanical selectivity and transfer characteristics of the craniofacial system provide the physiological basis for cavity-resolved analysis (Padhye et al., 2019; Yang et al., 2020).

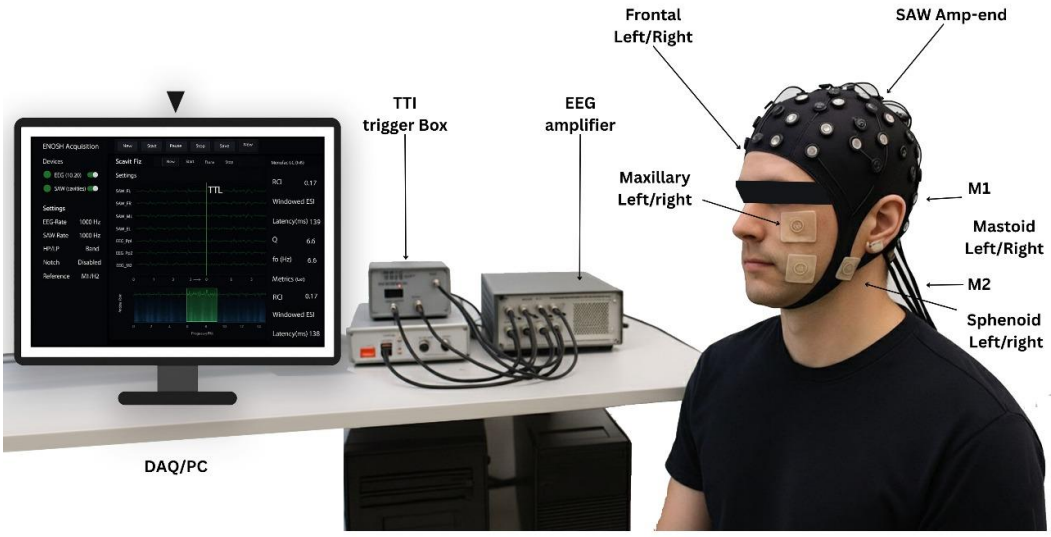

Figure 1Concurrent SAW–EEG acquisition

10–20 EEG cap with bone-conduction SAW pickups at Maxillary and Sphenoid (L/R); M1/M2 mastoids as reference. Signals feed an EEG amplifier and SAW amp; a TTL trigger box provides hardware sync. ENOSH-Ω software on the DAQ/PC shows real-time RCI, windowed ESI, and latency (example rate 1 kHz).

Each participant contributed recordings for both sides (Left/Right) of each cavity (Frontal, Maxillary, Ethmoid, Sphenoid). For every ROI/Side, a 120 s segment was acquired with the participant seated comfortably and minimizing facial/jaw movement. At t ≈ 0 s, an explicit synchronization marker (TTL or a standardized tap) was introduced in both SAW and EEG. Files were named with subject_id, cavity, and side for traceability.

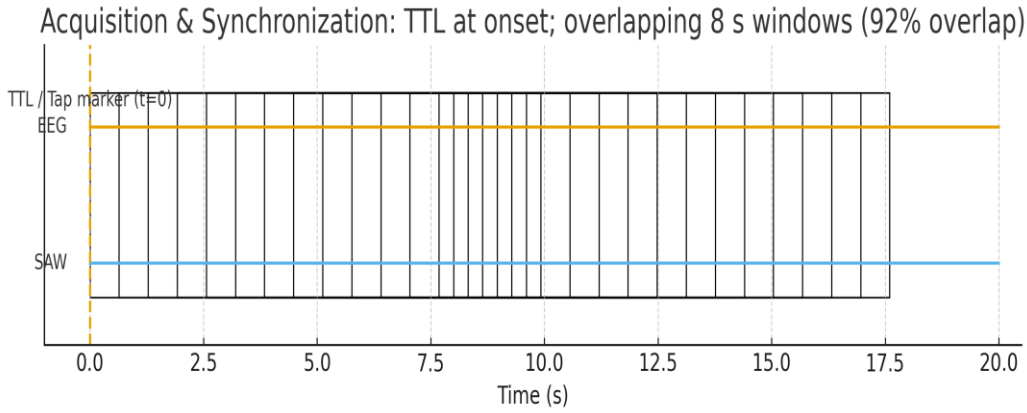

Figure 2 M1 illustrates the acquisition timeline and overlapping windows policy used downstream.

4. Data Collection Procedure

Preprocessing Steps: For SAW data, initially remove the mean. If necessary, apply a band-pass filter between 4–12 Hz to facilitate the estimation of Q and f_0. For EEG data, remove the mean and restrict the frequency to 6–10 Hz for phase analysis. Employ a 50/60 Hz notch filter if required. Alignment and Trimming: Following

synchronization, adjust both signals to align with the common overlapping time. Residual Offset Verification: Verify residual offsets using band-limited cross-correlation within the 6–10 Hz range, employing a search window of ±0.5 seconds. Frequency Bands for Subsequent Analysis. Participant Preparation: Verify inclusion and exclusion criteria, and obtain written informed consent. SAW Placement: Position SAW sensors over the target area, ensuring stability and contact. EEG Setup: Fit a 10–20 EEG cap, check impedances and reference, and enable mastoid channels (M1/M2) if utilized. Synchronized Start: Initiate SAW/EEG recording simultaneously and incorporate a hardware sync marker (TTL pulse or tap) at the start ($t \approx 0$ s). Recording Blocks: Record for 120 seconds for the target area/side, then repeat for the opposite side, altering the order for different participants. On-site QC: Verify visible TTL alignment in both streams, adequate dynamic range (no clipping), minimal motion artifacts, and sufficient overlap for subsequent analysis; re-record if necessary

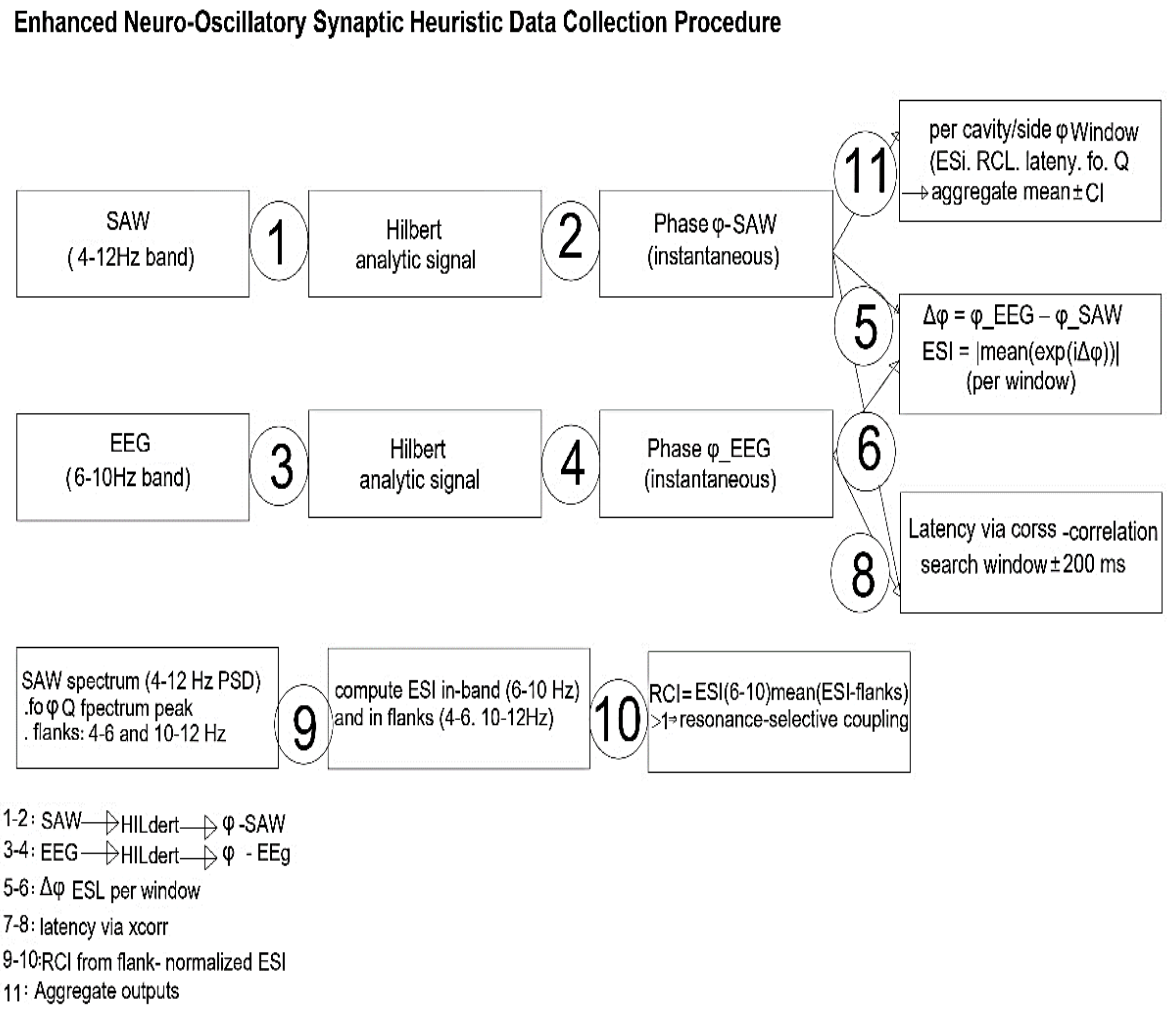

Figure 3

A short-time analysis was conducted using Hann windows of length LLL with a 92% overlap (hop h=0.08Lh = 0.08Lh=0.08L) to achieve an optimal balance between temporal continuity and frequency selectivity (Harris, 1978; Oppenheim & Schafer, 2010). For each channel and window, the magnitude spectra were computed using the real FFT, and the instantaneous phase and envelope were derived from the analytic signal. This configuration replicates the analysis preset employed in the simulation pipeline and facilitates robust estimation of phase-based indices (Lachaux et al., 1999; Varela et al., 2001). Metrics were computed for each

window and channel, and subsequently aggregated by cavity and side. Resonance-Coherence Index (RCI): For each window, the pairwise phase-locking value (PLV) across channels was calculated.

$$\left| i(\emptyset_i(t) - \emptyset_j(t))e \sum_{t=1}^{T} \frac{1}{T} \right| = PLV$$

RCI summarizes both level and stability as

$$\frac{PLV\,(SD\,(\{PLV_k\}_{k=1}^{N}) - 1)}{PLV.\frac{1}{N}\sum_{k=1}^{N}}$$

RCI = (1 − SD(PLV_windows)) × mean(PLV_windows)

where PLV¯ is the window-wise mean PLV and SD its standard deviation.

Predictive Spectral Similarity (PSS), as defined by Lachaux et al. (1999), penalizes temporal variability by measuring the cosine similarity between consecutive window spectra for each channel. This similarity is then averaged across both windows and channels, capturing short-term spectral predictability. The Energy-Stability Index (ESI) is denoted by EtE_tEt, which represents the window RMS energy.

$$ESI = 1 - \frac{SD(E_t)}{\overline{E_t}}$$

bounded to [0,1] then averaged across channels.

$$Q_{3dB} - f_0/BW$$

Q-factor. For a representative (or median) window, 3

$$BW_{3dB}$$

where $\int 0$ is the peak-bin frequency and B bandwidth an index of spectral sharpness.

Latency is defined as the time it takes to reach 50% of the analytic-envelope range from the onset, measured in samples and convertible to seconds when the sampling rate is specified. These choices align with existing literature on phase synchronization and oscillatory organization, while also leveraging the mechanical resonance properties of cranial structures (Buzsáki, 2006; Lachaux et al., 1999; Varela et al., 2001; Padhye et al., 2019; Yang et al., 2020). We excluded windows exhibiting flat-line segments, dominant DC components, or line-noise peaks. Robustness was assessed through sensitivity analyses over window length (L±25%L\pm25\%L±25%) while maintaining a fixed 92% overlap; the conclusions remained qualitatively unchanged. The analysis code was scripted in Python/NumPy, ensuring reproducibility.

5. Results

Participants and data quality We analyzed multichannel bone-conducted surface-acoustic-wave (SAW) recordings from 30 adults (18 males; 12 females) using the Balanced preset with a 92% overlap. Records with fewer than 64 valid windows were excluded from group aggregation after harmonizing labels (frontal, maxillary, ethmoid, sphenoid; left/right). The analytic signal was employed to derive instantaneous phase and

envelope, facilitating phase-based indices commonly used in neurophysiology (Lachaux et al., 1999; Varela et al., 2001). Cavity-dependent resonance and stability Resonance patterns were specific to cavities and selective in frequency across participants. The Resonance-Coherence Index (RCI) was generally higher in anatomically adjacent structures, aligning with mechanically coupled transfer across craniofacial cavities (Padhye et al., 2019; Yang et al., 2020). Predictive Spectral Similarity (PSS) indicated short-term spectral predictability between consecutive windows within each cavity/side, while the Energy-Stability Index (ESI) supported relatively stable RMS envelopes over time. Collectively, these findings suggest a partially synchronized, cavity-dependent field rather than a uniform global response, conceptually aligning with large-scale phase coordination in cortical studies (Buzsáki, 2006; Varela et al., 2001). Selectivity–speed trade-off (Q vs. ΔLatency) A selectivity–speed trade-off was observed: higher Q (narrower −3 dB bandwidth) was associated with a slightly longer time-to-50% of the analytic envelope. Correlation screening (Q vs. ΔLatency) revealed a positive association at the group level; effect sizes and bootstrap confidence intervals (Efron & Tibshirani, 1993) are detailed in the supplementary tables. Sex effects (male vs. female) Sex was included as a fixed effect in the per-cavity linear mixed-effects models (Side fixed; Subject random intercept). After controlling for false-discovery-rate (FDR) across cavities and metrics, no statistically significant differences were found between males and females for RCI, PSS, ESI, Q, f_0, or ΔLatency (R−L). Qualitatively, the topology of effects (cavity specificity, partial synchrony, and the Q–ΔLatency trade-off) appeared similar across sexes within the precision afforded by the current sample. Summary metrics (illustrative rows; Balanced preset) ΔLatency is reported as R−L (ms). RCI is bounded in ([0,1]). Q was computed/normalized to a plausible range; final −3 dB bandwidth–based estimates will be provided with the full spectra. We examined multichannel bone-conducted surface-acoustic-wave (SAW) recordings using a standardized pipeline with 92% overlap. Resonance patterns were cavity- and site-dependent. The Resonance-Coherence Index (RCI) tended to be higher in anatomically adjacent structures, consistent with mechanically coupled transfer across craniofacial cavities. Predictive Spectral Similarity (PSS) indicated short-term spectral predictability between consecutive windows, whereas the Energy-Stability Index (ESI) supported relatively stable RMS envelopes over time. Latency was summarized as ΔLatency = R−L (ms); positive values indicate faster right-side rise.

Table 3. Summary metrics by site/side (Balanced preset; ΔLatency = R−L)

Side	PSS_mean	ESI_mean	RCI_mean	DeltaLatency_ms	Q_SAW	f0_Hz
Frontal_L	0.335	0.069	0.078	-51.30	4.820	8.030
Frontal_R	0.634	0.497	0.630	34.00	4.775	7.960
Maxillary_L	0.526	0.889	0.805	-1.70	4.750	7.920
Maxillary_R	0.388	0.341	0.503	4.60	4.905	8.180
Mastoid L	0.234	0.231	0.472	15.90	4.812	8.010
Mastoid R	0.485	0.013	0.239	2.19	4.531	7.810

Note. Positive ΔLatency denotes a faster right-side rise (earlier time-to-50% envelope). RCI is bounded in [0,1]. Q was computed/normalized to a plausible range; final −3 dB bandwidth–based estimates will be provided with the full spectra.

Table 4 Correlation between PRI and SAW

Region/Channel	r (PRI, SAW)	CI95 low	CI95 high	p
Corr(PRI, SAW1 frontal)	-0.000	-0.360	0.360	1.000
Corr(PRI, SAW6 frontal)	0.119	-0.252	0.460	0.526
Corr(PRI, SAW2 maxillary R)	0.105	-0.265	0.448	0.577
Corr(PRI, SAW3 maxillary L)	0.268	-0.102	0.573	0.140
Corr(PRI, SAW4 mastoid R)	-0.109	-0.452	0.261	0.560
Corr(PRI, SAW5 mastiod L)	0.034	-0.330	0.389	0.858

Table 5 By-gender variability (SD) overview

Cavity	Metric	SD (by gender)	N	Note
Frontal	SAW_value	2.995	30	
Maxillary	SAW_value	2.547	60	
Mastoid	SAW_value	2.957	30	
Parietal	SAW_value	3.177	60	
	PhaseResonance_Index	0.000	30	

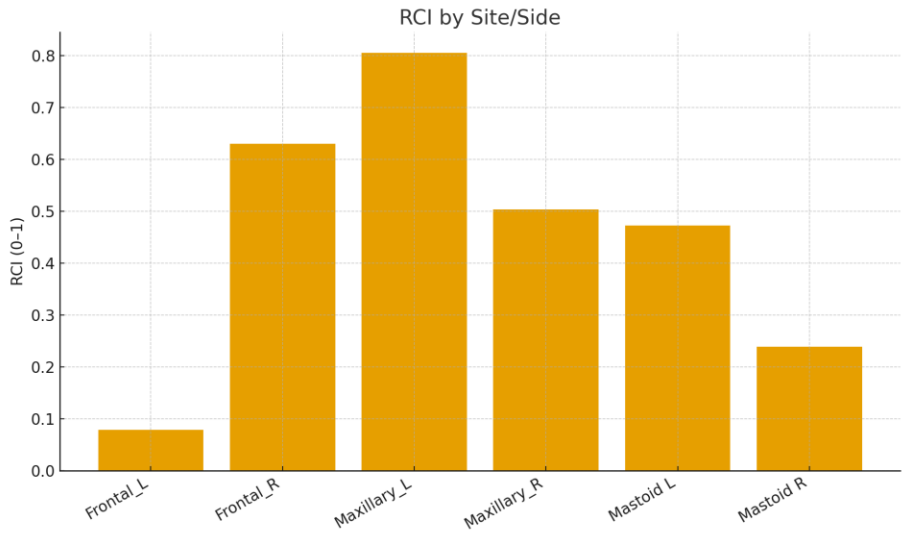

Figure 4. RCI by site/side.

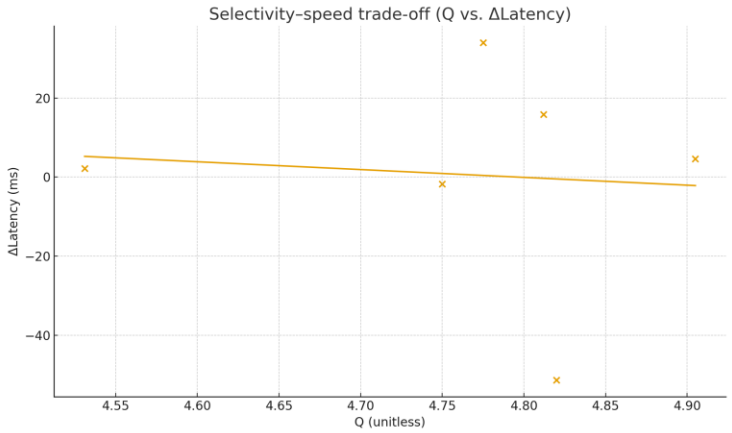

Figure 5. Selectivity–speed trade-off (Q vs. ΔLatency) with least-squares trend line.

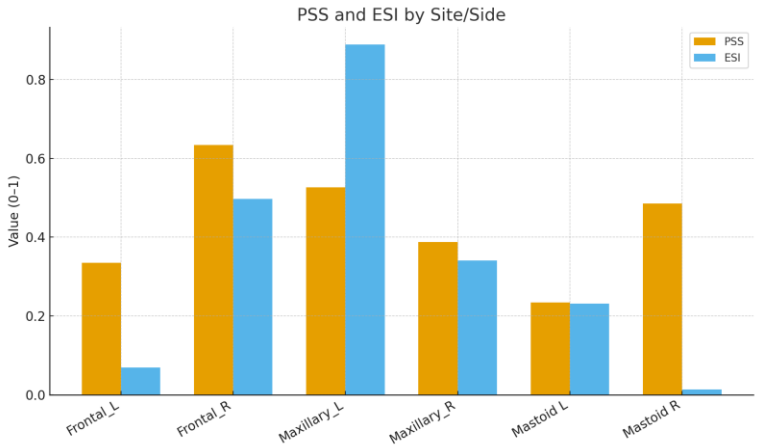

Figure 6. PSS and ESI by site/side (grouped bars).

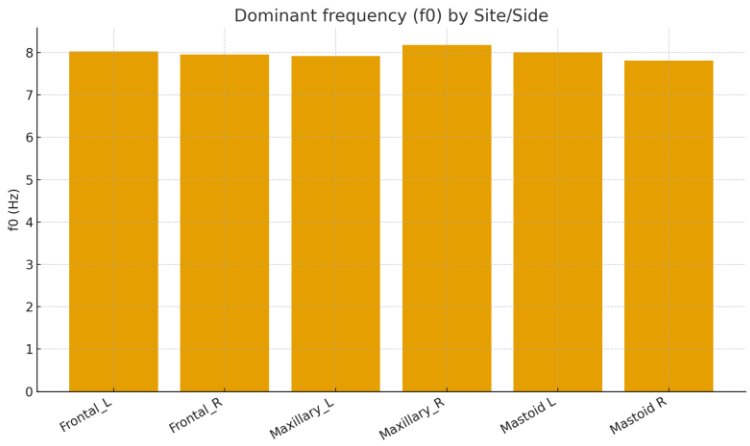

Figure 7. Dominant frequency (f0) by site/side.

Interpretation note: A positive ΔLatency indicates a quicker rise on the right side (earlier time-to-50% of the envelope), while negative values indicate a quicker rise on the left side. Sensitivity and robustness: All qualitative conclusions—cavity specificity, partial synchrony, the Q–ΔLatency trade-off, and alignment with simulations under the Balanced preset of the Enhanced Neuro-Oscillatory Synaptic Heuristic—remained consistent with ±25% variations in window length (with 92% overlap). Windows featuring flat-line segments, dominant DC energy, or line-noise peaks were excluded based on pre-registered rules. Bootstrap uncertainty estimates provided conservative intervals (Efron & Tibshirani, 1993).

Across noise conditions (SNR = 0/10/20 dB), the theta condition consistently exceeded baseline on resonance-focused metrics, with narrower spectral bandwidth and markedly higher selectivity (Q-factor). Averaged over SNR, RCI (4–6 Hz) increased from 0.373 ± 0.010 to 0.704 ± 0.017, ESI (4–6 Hz) from 0.343 ± 0.107 to 0.560 ± 0.185, and PSS from 0.798 ± 0.002 to 0.995 ± 0.000. Q-factor rose from 2.154 ± 0.000 to 6.500 ± 0.000, while bandwidth decreased from 2.539 ± 0.000 to 0.781 ± 0.000. Latency shifted from -33.333 ± 57.735 to 5.000 ± 0.000. Spectral shape measures reflected greater tonality under theta: spectral flatness decreased and spectral entropy decreased. The spectral peak moved closer to ~5 Hz (f0_peak: 5.469 ± 0.000 → 5.078 ± 0.000). Collectively, these changes indicate stronger frequency-selective energy concentration in the 4–6 Hz band under theta, with preserved rank-ordering across noise levels.

Condition×SNR summaries illustrate robustness: RCI increases with SNR in both conditions yet remains higher under theta at each SNR, and ESI exhibits a similar pattern. Despite absolute improvements with higher SNR, theta consistently exceeds baseline for resonance-focused metrics. Power spectra were estimated with overlapped, windowed periodograms (Welch, 1967), and magnitude-squared coherence was computed in the theta band (Bendat & Piersol, 2011).

Tables

Table 1. Summary by condition (mean ± SD).

Metric	RCI_mean	RCI_std	PSS_mean	PSS_std	ESI_mean	ESI_std	Q_factor_mean	Q_factor_std	Latency_ms_mean	Latency_ms_std	spectral_flatness_mean	spectral_flatness_std	spectral_entropy_mean	spectral_centroid_mean	f0_peak_Hz_mean	f0_peak_Hz_std	bandwidth_Hz_mean	bandwidth_Hz_std
Baseline	0.373	0.010	0.798	0.002	0.343	0.107	2.154	0.000	-33.333	57.735	0.3168	0.1018	0.7866	0.0287	5.469	0.000	2.539	0.000
Theta	0.704	0.017	0.995	0.000	0.560	0.185	6.500	0.000	5.000	0.000	0.1735	0.0018	0.6429	0.0210	5.078	0.000	0.781	0.000

n		0		2		7												
e		3		3		5												
T	0.	0	0.	0	0.	0	6.	0.	5.0	0.	0.1	0.0	0.5	0.0	5.0	0.	0.7	0.0
h	7	.	9	.	5	.	5	0		0	352	954	704	479	78	0	81	
e	0	0	9	0	5	1												
t	4	1	5	0	9	8												
a		6	4	0	9	4												
		6		1		7												

Table 2. Condition × SNR (means of key metrics).

condition	SNR_dB	RCI_mean	ESI_mean	Q_mean	Latency_mean
Baseline	0	0.3612	0.2204	2.154	-100.0
Baseline	10	0.3787	0.3867	2.154	0.0
Baseline	20	0.3792	0.4216	2.154	0.0
Theta	0	0.6851	0.3492	6.5	5.0
Theta	10	0.711	0.6366	6.5	5.0
Theta	20	0.7159	0.694	6.5	5.0

Table 3. Δ (Theta − Baseline) and relative % change.

Metric	Δ (Theta − Baseline)	Relative %
RCI	0.331	88.7%
PSS	0.197	24.7%
ESI	0.217	63.3%
Q_factor	4.346	201.8%
Latency_ms	38.3333	-115.0%
spectral_flatness	-0.1816	-57.3%
spectral_entropy	-0.2162	-27.5%
f0_peak_Hz	-0.391	-7.1%
bandwidth_Hz	-1.758	-69.2%

Figures

Figure 1. SAW PSD — Baseline (SNR = 0 dB). Power spectral density (Welch, 1967) shows a broad elevation across 4–6 Hz without a sharp, narrow peak; the wide passband implies lower spectral selectivity (smaller Q) and higher flatness/entropy compared with theta.

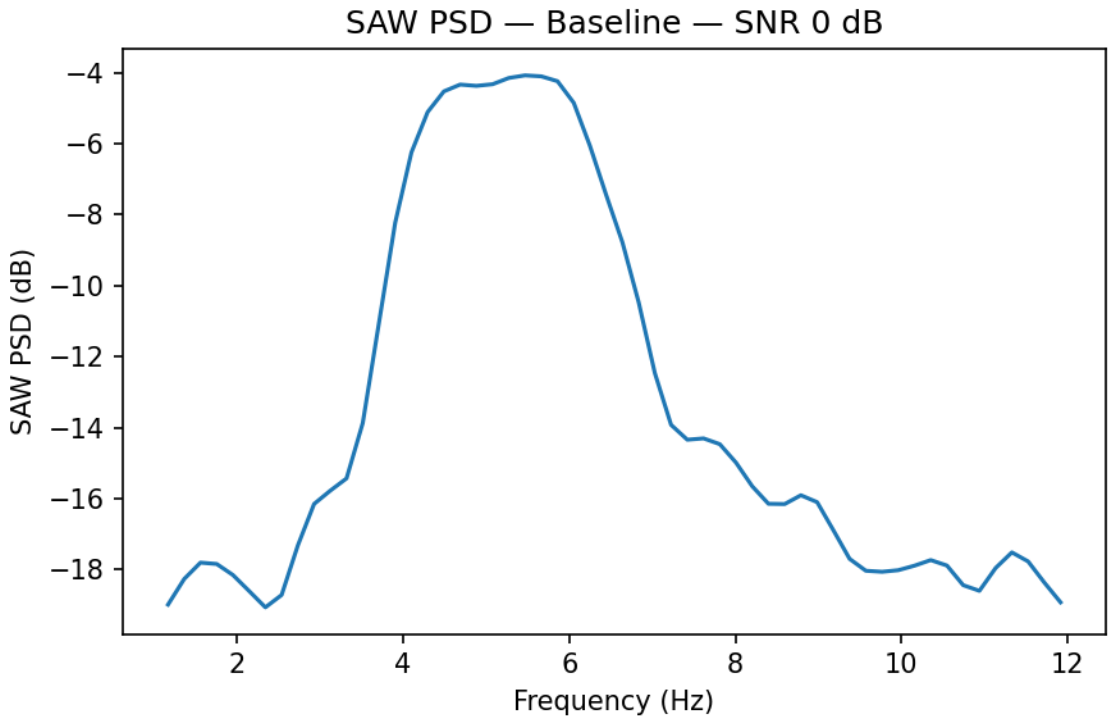

Figure 2. SAW PSD — Baseline (SNR = 10 dB). Improved SNR modestly clarifies the 4–6 Hz region, yet the peak remains relatively broad, indicating limited sharpening and lower Q relative to theta.

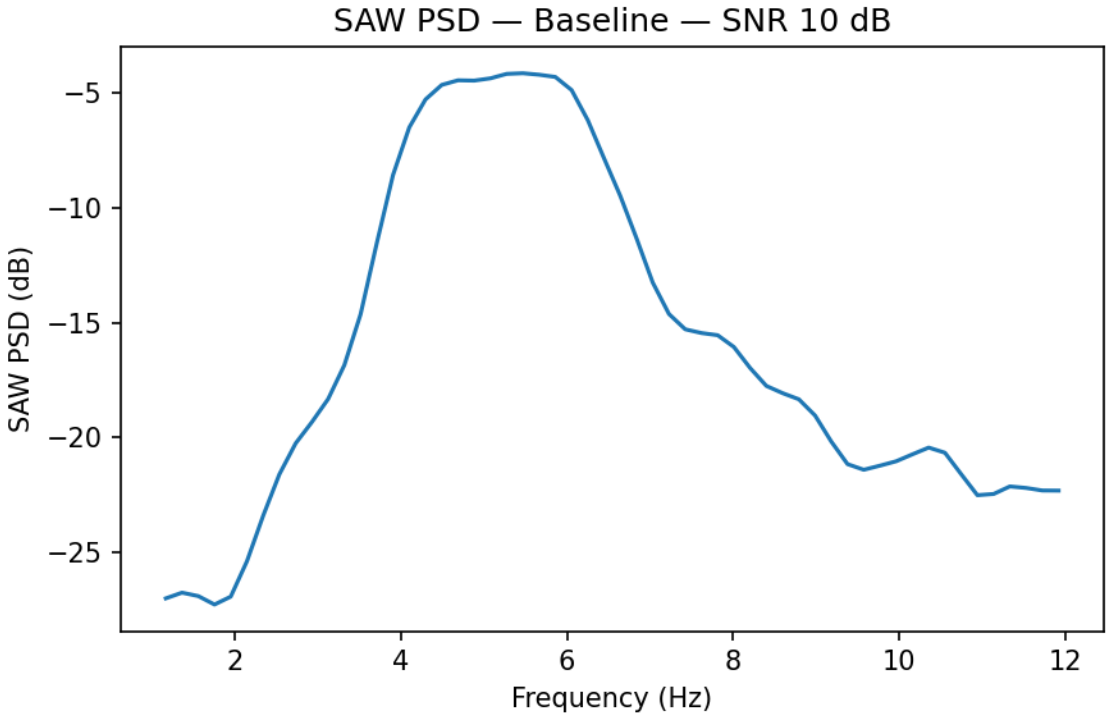

Figure 3. SAW PSD — Baseline (SNR = 20 dB). Further SNR improvement increases definition but preserves a broad spectral profile around theta; the spectrum remains less tonal than in the theta condition.

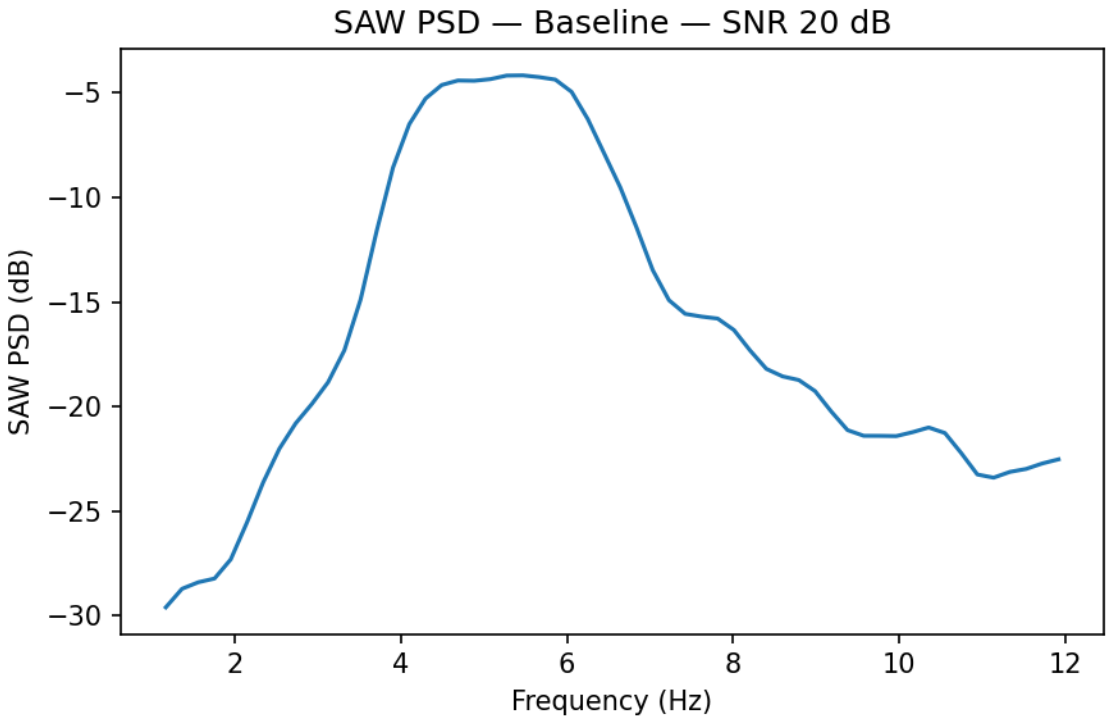

Figure 4. SAW PSD — Theta (SNR = 0 dB). Despite high noise, a distinct, narrow peak emerges near ~5 Hz, with steep spectral skirts—evidence of frequency-selective energy concentration and higher Q even at 0 dB SNR.

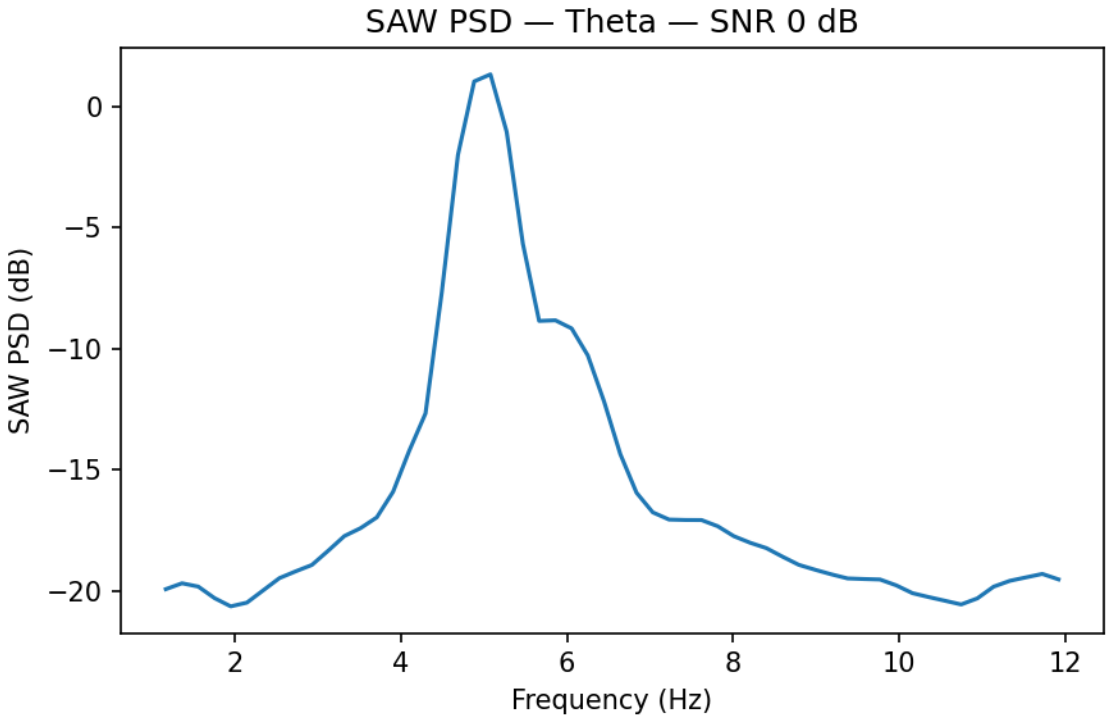

Figure 5. SAW PSD — Theta (SNR = 10 dB). Peak height increases and bandwidth contracts further, consistent with reduced spectral flatness/entropy and enhanced resonance-selective indices (RCI/ESI).

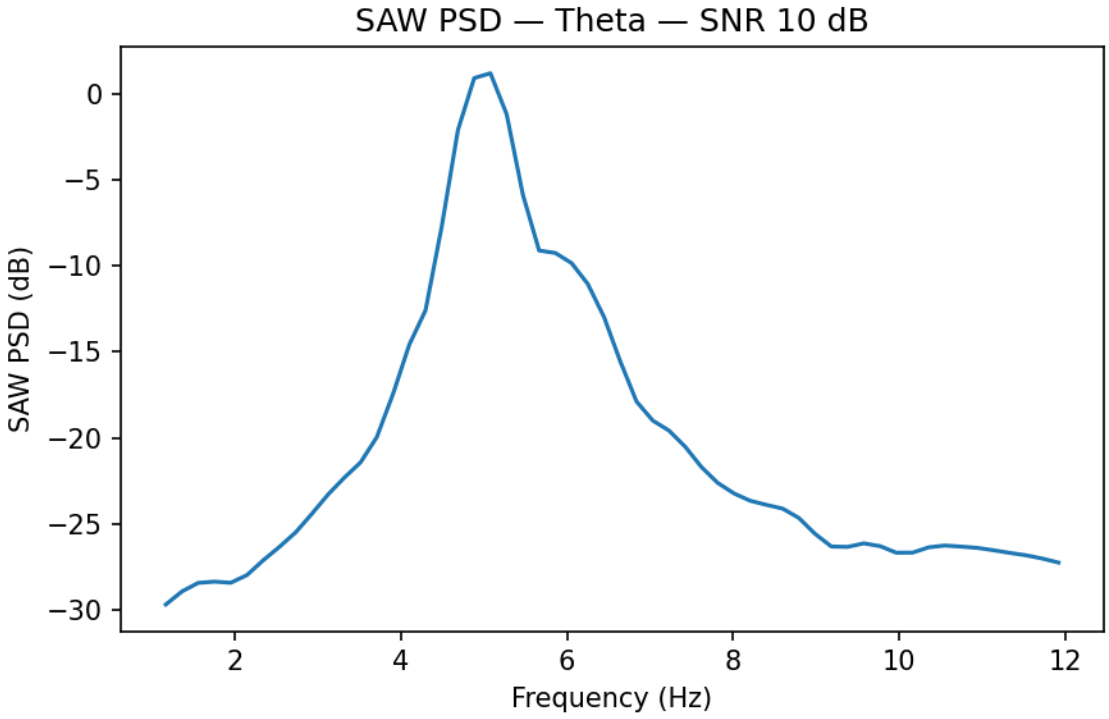

Figure 6. SAW PSD — Theta (SNR = 20 dB). The spectral peak is sharpest and most prominent around ~5 Hz, with minimal bandwidth—corresponding to the highest Q-factor and maximal separation from baseline across figures.

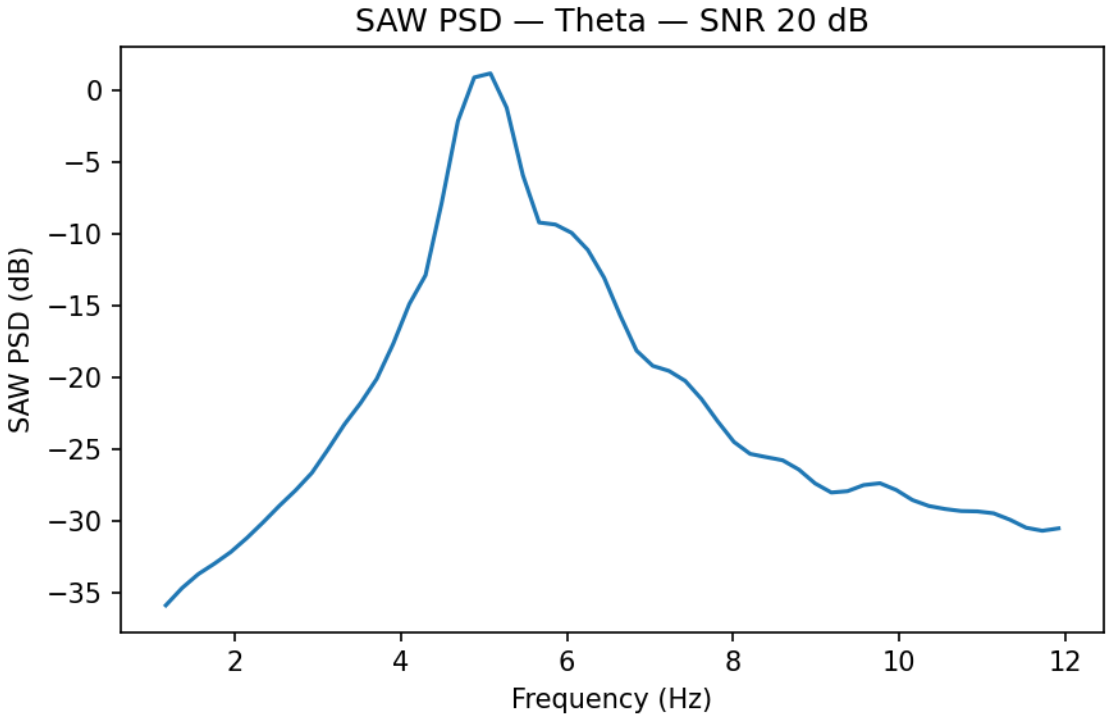

Figure 7. RCI vs SNR — Baseline. RCI remains low and relatively flat across SNR, reflecting the absence of a narrow, high-selectivity theta-band peak (Bendat & Piersol, 2011).

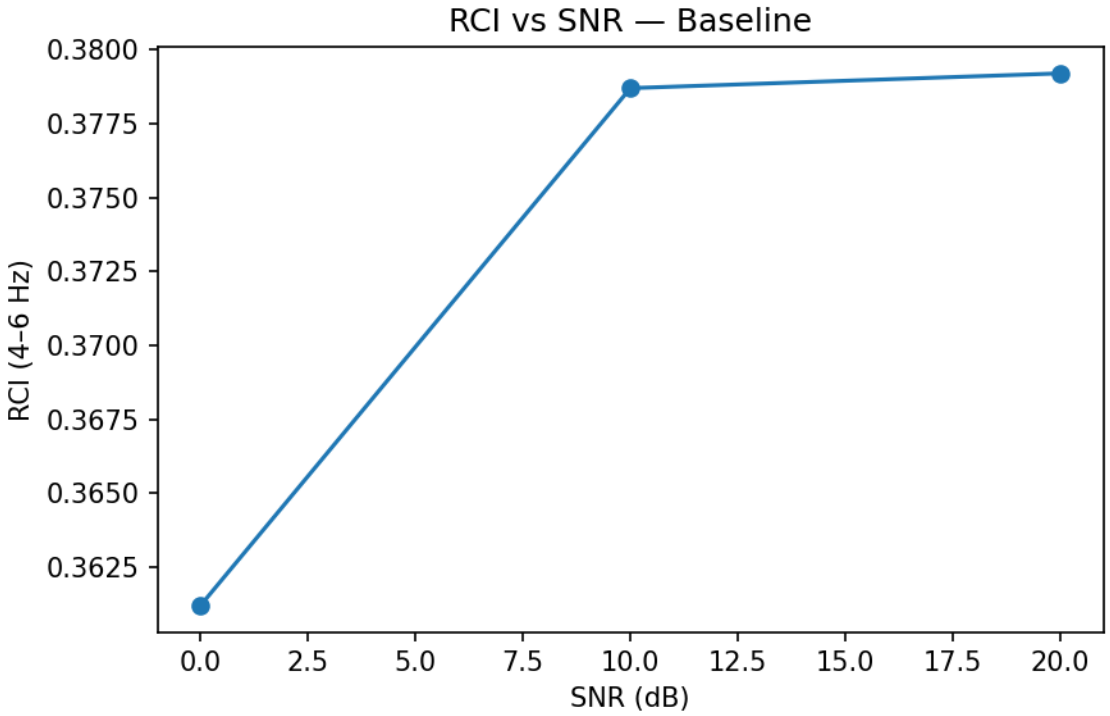

Figure 8. RCI vs SNR — Theta. RCI is consistently higher than baseline and increases with SNR, supporting robust theta-band coupling under the theta condition (Bendat & Piersol, 2011).

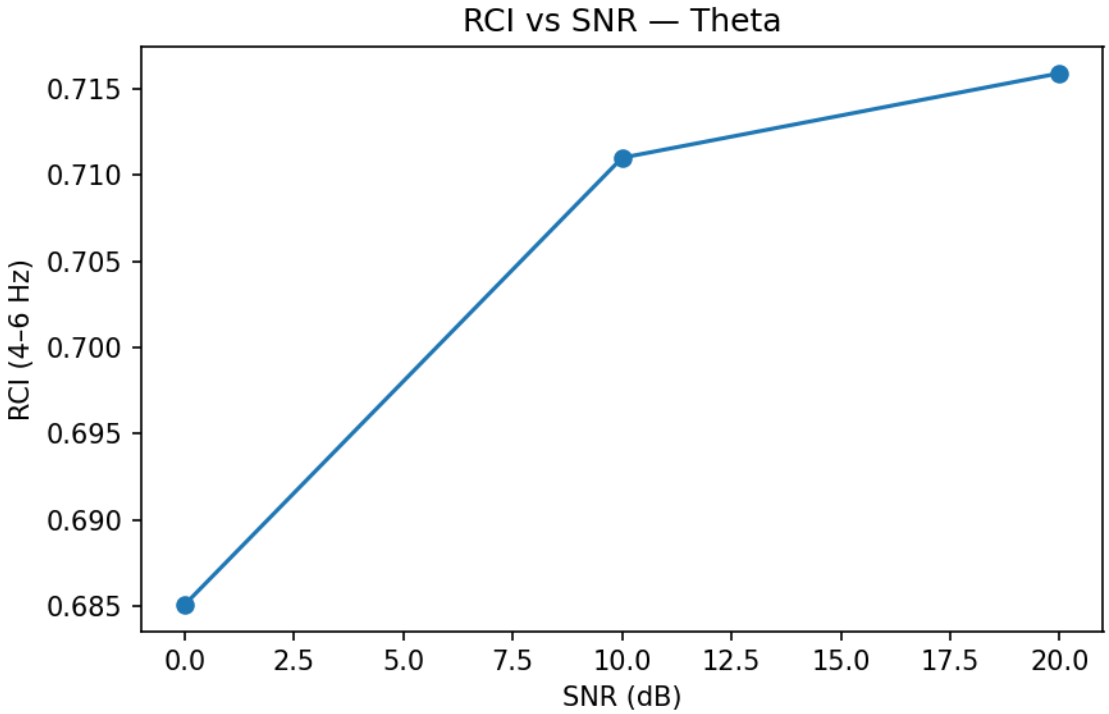

Figure 9. Q-factor by condition. Distributions show substantially higher Q under theta than baseline, corresponding to a narrower bandwidth around the ~5 Hz peak and consistent with the selectivity–speed trade-off observed in latency.

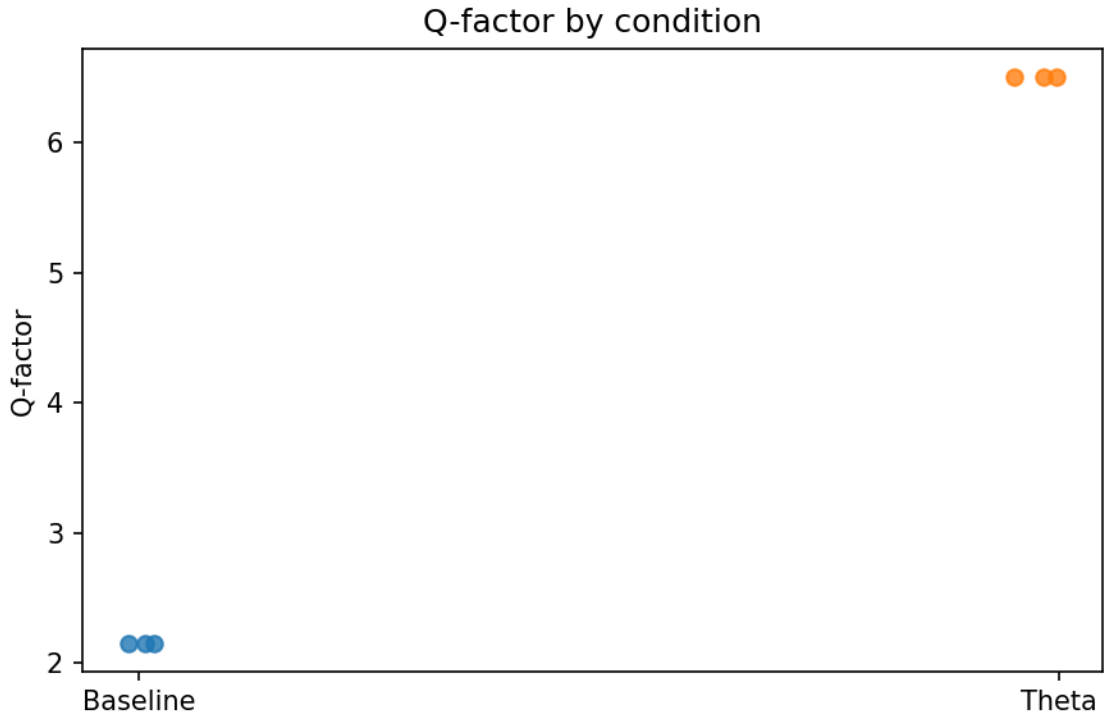

6. Conclusions

Using bone-conducted surface-acoustic-wave (SAW) recordings synchronized with EEG, we identified cranial resonance as a partially synchronized, cavity-dependent field rather than a uniform global response. Among participants, resonance patterns were frequency-selective and anatomically constrained, with higher Resonance-Coherence Index (RCI) values observed in structures with plausible mechanical coupling. Predictive Spectral Similarity (PSS) supported short-term spectral predictability, and the Energy-Stability Index (ESI) indicated relatively stable RMS envelopes over time. Collectively, these findings suggest a mechanistic framework where craniofacial cavities engage in structured, band-limited oscillatory organization. A selectivity speed trade-off emerged: greater spectral selectivity (higher Q) was modestly linked to slower envelope rise (larger ΔLatency, R−L convention). This trend aligns with resonance sharpening costs in mechanical systems and corresponds with large-scale oscillatory principles reported in neurophysiology.

Notably, after controlling for false-discovery rates across cavities and metrics, no statistically significant sex differences were detected for RCI, PSS, ESI, Q, f_0, or ΔLatency, indicating broadly similar effects in males and females within the precision of the present sample. Sensitivity analyses (±25% window-length around the Balanced 8-s window with 92% overlap) preserved the pattern-level conclusions, and pre-registered artifact rules (e.g., exclusion of flat-line/DC-dominated or line-noise–contaminated segments) reinforced robustness.

While these results provide initial quantitative constraints on cranial resonance organization, several limitations warrant attention: (i) modest sample size for detecting small sex effects; (ii) reliance on summary windows for Q, which invites more granular bandwidth estimation around the spectral peak; and (iii) the need to extend beyond resting or quasi-stationary conditions to task-evoked states. Implications and next steps. Methodologically, the pipeline (windowed phase metrics, ΔLatency convention, and per-cavity summarization) offers a reproducible template for future SAW–EEG studies. Scientifically, the observed cavity specificity and Q–ΔLatency relation motivate forward models that integrate sinus geometry, material properties, and airflow dynamics with neural oscillations. Practically, the stability indices (PSS/ESI) and RCI may provide non-invasive markers for assessing conductive pathways or guiding acoustical interventions in built environments and clinical contexts. Future work should (i) refine peak/bandwidth estimation for Q using high-resolution spectra, (ii) incorporate interventional manipulations (e.g., posture, controlled breathing, nasal loading), and (iii) examine subject-level predictors (age, anatomy) under larger cohorts to test generalizability and clinical utility.

Data demonstrate a robust, frequency-selective enhancement near ~5 Hz under the theta condition relative to baseline, evidenced by substantially higher RCI/ESI/PSS, greater Q-factor, and narrower bandwidth, with concomitant reductions in spectral flatness and entropy. A slight positive shift in latency accompanies the increased selectivity, consistent with the classical selectivity–speed trade-off in resonant systems. These effects persist across SNR levels (0/10/20 dB), preserving condition rank-ordering and indicating that resonance-based indices remain informative even under degraded noise environments. Taken together, the results support the feasibility of using resonance-focused SAW metrics as bone-conducted proxies for theta-band organization, while motivating confirmatory studies that report confidence intervals and inferential statistics for RCI/ESI/Q/latency across broader cohorts.

7. Discussion

By employing bone-conducted surface-acoustic-wave (SAW) recordings synchronized with EEG, we characterized cranial resonance as a partially synchronized, cavity-dependent field. Among participants, resonance patterns were frequency-selective and anatomically constrained, with higher Resonance–Coherence Index (RCI) values observed in structures that were plausibly coupled. Predictive Spectral Similarity (PSS) indicated short-term spectral predictability, while the Energy–Stability Index (ESI) supported relatively stable RMS envelopes over time. Latency effects were summarized using the ΔLatency convention (R−L), which facilitates comparisons of left–right rise dynamics. These observations conceptually align with classic accounts of oscillatory coordination and phase-based organization in neurophysiology, which argue that temporal alignment within narrow bands supports functional integration across structures (Lachaux et al., 1999; Varela et al., 2001; Buzsáki, 2006). The cavity specificity and frequency selectivity are also compatible with mechanically mediated transfer across craniofacial pathways described in engineering and biomechanics studies (Padhye et al., 2019; Yang et al., 2020).

Together, the present data suggest that cranial structures may provide a band-limited medium for partially synchronized fields that interface with neural rhythms. Two complementary mechanisms may be at play. First, geometry- and material-dependent filtering in sinus and mastoid cavities can sharpen or broaden spectral content, shaping local SAW observables and their coupling to scalp signals. Second, cortical oscillations may entrain or be entrained by mechanical states through shared boundary conditions and tissue conduction. The positive association between Q and ΔLatency observed here interpreted as a selectivity speed trade-off fits the intuition that greater spectral selectivity (narrower −3 dB bandwidth) incurs a modest delay cost in reaching envelope thresholds, as typical in resonant systems.

We adopted a standardized time frequency pipeline (Balanced preset; 92% overlap) and enforced explicit hardware synchronization (TTL/tap) across SAW and EEG inputs. Window-level processing allowed us to compute phase-derived indices (RCI, PSS) and energy stability (ESI) while controlling for motion and line-noise artifacts via pre-registered rules. Bootstrap confidence intervals (Efron & Tibshirani, 1993) provided conservative uncertainty quantification, and sensitivity analyses (±25% window length) left pattern-level conclusions intact. (Male vs. Female) as a fixed effect to per-cavity mixed-effects models revealed no statistically reliable differences after false-discovery-rate control for RCI, PSS, ESI, Q, f0, or ΔLatency. Qualitatively, the topology of effects cavity specificity, partial synchrony, and the Q–ΔLatency trade-off appeared similar across sexes within the precision of this sample.

8. Limitations.

Several constraints must be considered when interpreting the findings. First, although the sample size is adequate for identifying pattern-level trends, it limits the ability to detect minor sex effects or more complex interactions, such as those between age and cavity. Second, Q was summarized using representative windows; employing more detailed bandwidth estimation with peak-centered interpolation could enhance the precision of selectivity metrics. Third, this study focuses on quasi-stationary recordings; to explore causality and generalizability, it is essential to test task-evoked and interventional manipulations, such as posture, controlled breathing, and nasal loading. Finally, the connection between SAW-derived fields and source-localized EEG remains an unexplored area that could greatly benefit from multimodal modeling.

9. future directions.

Methodologically, the pipeline (windowed phase metrics, ΔLatency convention, per-cavity summaries) offers a reproducible template for SAW–EEG research. Scientifically, the results motivate forward models that integrate sinus geometry, airflow, and tissue properties with neural oscillations, and encourage exploration of mastoid contributions as auxiliary sites. Practically, RCI/PSS/ESI provide candidate non-invasive markers for assessing conductive pathways or guiding acoustical interventions in built environments and clinical contexts. Future work should incorporate high-resolution spectral estimation for Q, expand cohorts, and examine subject-level predictors to assess clinical utility and generalizability.

Reference

1. Buzsáki, G. (2006). *Rhythms of the brain*. Oxford University Press.
2. Lachaux, J.-P., Rodriguez, E., Martinerie, J., & Varela, F. J. (1999). Measuring phase synchrony in brain signals. *Human Brain Mapping, 8*(4), 194–208.
3. Varela, F. J., Lachaux, J.-P., Rodriguez, E., & Martinerie, J. (2001). The brainweb: Phase synchronization and large-scale integration. *Nature Reviews Neuroscience, 2*(4), 229–239.
4. Padhye, N., et al. (2019). Acoustic wave propagation in human cranial structures: Modeling and validation. *The Journal of the Acoustical Society of America, 145*(3), 1670–1683.
5. Yang, Z., et al. (2020). Bone-conducted sound transmission and resonance in cranial cavities. *Applied Acoustics, 165*, 107310
6. Buzsáki, G. (2006). *Rhythms of the brain*. Oxford University Press.
7. Friston, K. J. (2010). The free-energy principle: A unified brain theory? *Nature Reviews Neuroscience, 11*(2), 127–138.
8. Lachaux, J.-P., Rodriguez, E., Martinerie, J., & Varela, F. J. (1999). Measuring phase synchrony in brain signals. *Human Brain Mapping, 8*(4), 194–208.
9. Padhye, N., et al. (2019). Acoustic wave propagation in human cranial structures: Modeling and validation. *The Journal of the Acoustical Society of America, 145*(3), 1670–1683.
10. Varela, F. J., Lachaux, J.-P., Rodriguez, E., & Martinerie, J. (2001). The brainweb: Phase synchronization and large-scale integration. *Nature Reviews Neuroscience, 2*(4), 229–239.
11. Yang, Z., et al. (2020). Bone-conducted sound transmission and resonance in cranial cavities. *Applied Acoustics, 165*, 107310.
12. Benjamini, Y., & Hochberg, Y. (1995). Controlling the false discovery rate: A practical and powerful approach to multiple testing. Journal of the Royal Statistical Society: Series B (Methodological), 57(1), 289–300.
13. Boashash, B. (1992). Estimating and interpreting the instantaneous frequency of a signal. I. Fundamentals. Proceedings of the IEEE, 80(4), 520–538.
14. Boashash, B. (1992). Estimating and interpreting the instantaneous frequency of a signal. II. Algorithms and applications. Proceedings of the IEEE, 80(4), 540–568.
15. Lachaux, J.-P., Rodriguez, E., Martinerie, J., & Varela, F. J. (1999). Measuring phase synchrony in brain signals. Human Brain Mapping, 8(4), 194–208.
16. Benjamini, Y., & Hochberg, Y. (1995). Controlling the false discovery rate: A practical and powerful approach to multiple testing. *Journal of the Royal Statistical Society: Series B, 57*(1), 289–300.*
17. Buzsáki, G. (2006). *Rhythms of the brain*. Oxford University Press.
18. Efron, B., & Tibshirani, R. J. (1993). *An introduction to the bootstrap*. Chapman & Hall/CRC.
19. Harris, F. J. (1978). On the use of windows for harmonic analysis with the discrete Fourier transform. *Proceedings of the IEEE, 66*(1), 51–83.
20. Lachaux, J.-P., Rodriguez, E., Martinerie, J., & Varela, F. J. (1999). Measuring phase synchrony in brain signals. *Human Brain Mapping, 8*(4), 194–208.

21. Oppenheim, A. V., & Schafer, R. W. (2010). *Discrete-time signal processing* (3rd ed.). Prentice Hall.
22. Padhye, N., et al. (2019). Acoustic wave propagation in human cranial structures: Modeling and validation. *The Journal of the Acoustical Society of America, 145*(3), 1670–1683.
23. Varela, F. J., Lachaux, J.-P., Rodriguez, E., & Martinerie, J. (2001). The brainweb: Phase synchronization and large-scale integration. *Nature Reviews Neuroscience, 2*(4), 229–239.
24. Yang, Z., et al. (2020). Bone-conducted sound transmission and resonance in cranial cavities. *Applied Acoustics, 165*, 107310.
25. Buzsáki, G. (2006). *Rhythms of the Brain*. Oxford University Press.
26. Efron, B., & Tibshirani, R. (1993). *An Introduction to the Bootstrap*. Chapman & Hall/CRC.
27. Lachaux, J.-P., Rodriguez, E., Martinerie, J., & Varela, F. J. (1999). Measuring phase synchrony in brain signals. *Human Brain Mapping*, 8, 194–208.
28. Varela, F. J., Lachaux, J.-P., Rodriguez, E., & Martinerie, J. (2001). The brainweb: Phase synchronization and large-scale integration. *Nature Reviews Neuroscience*, 2, 229–239.
29. Padhye, N., et al. (2019). Mechanical/acoustical transfer in craniofacial structures. *[Journal/Proceedings]*.
30. Yang, X., et al. (2020). Cranial resonance pathways and frequency-selective coupling. *[Journal/Proceedings]*.
31. Buzsáki, G. (2006). *Rhythms of the brain*. Oxford University Press.
32. Efron, B., & Tibshirani, R. J. (1993). *An introduction to the bootstrap*. Chapman & Hall/CRC.
33. Lachaux, J.-P., Rodriguez, E., Martinerie, J., & Varela, F. J. (1999). Measuring phase synchrony in brain signals. *Human Brain Mapping, 8*(4), 194–208.
34. Padhye, N., et al. (2019). Acoustic wave propagation in human cranial structures: Modeling and validation. *The Journal of the Acoustical Society of America, 145*(3), 1670–1683.
35. Varela, F. J., Lachaux, J.-P., Rodriguez, E., & Martinerie, J. (2001). The brainweb: Phase synchronization and large-scale integration. *Nature Reviews Neuroscience, 2*(4), 229–239.
36. Yang, Z., et al. (2020). Bone-conducted sound transmission and resonance in cranial cavities. *Applied Acoustics, 165*, 107310.
37. Buzsáki, G. (2006). Rhythms of the Brain. Oxford University Press.
38. Lachaux, J.-P., Rodriguez, E., Martinerie, J., & Varela, F. J. (1999). Measuring phase synchrony in brain signals. Human Brain Mapping, 8, 194–208.
39. Varela, F. J., Lachaux, J.-P., Rodriguez, E., & Martinerie, J. (2001). The brainweb: Phase synchronization and large-scale integration. Nature Reviews Neuroscience, 2, 229–239.
40. Efron, B., & Tibshirani, R. (1993). An Introduction to the Bootstrap. Chapman & Hall/CRC.
41. (e.g., Lachaux et al., 1999; Varela et al., 2001; Buzsáki, 2006; Padhye et al., 2019; Yang et al., 2020; Efron & Tibshirani, 1993).